Chemical Science

ROYAL SOCIETY OF CHEMISTRY

EDGE ARTICLE

View Article Online
View Journal | View Issue

Cite this: *Chem. Sci.*, 2022, **13**, 4566

All publication charges for this article have been paid for by the Royal Society of Chemistry

Reversible inhibition of the oxidase-like activity of Fe single-atom nanozymes for drug detection†

Weiwei Wu,[ab] Liang Huang,[a] Xinyang Zhu,[ab] Jinxing Chen,[ab] Daiyong Chao,[a] Minghua Li,[a] Shuangli Wu[ab] and Shaojun Dong *[ab]

Received 12th January 2022
Accepted 19th March 2022

DOI: 10.1039/d2sc00212d

rsc.li/chemical-science

Mechanism research of nanozymes has always been of great interest since their emergence as outstanding mimics of friable natural enzymes. An important but rarely mentioned issue in mechanism research of nanozymology is the inhibitory effect of nanozymes. And conventional nanozymes with various active sites hinder the mechanism research, while single-atom Fe–N–C nanozymes with similar active sites to natural enzymes exhibit structural advantages. Herein, we synthesized Fe single-atom nanozymes (Fe-SANs) with ultrahigh oxidase-like activity and found that a common analgesic-antipyretic drug 4-acetamidophenol (AMP) had inhibitory effects for the oxidase-like activity of Fe-SANs. We investigated the inhibitory effects in detail and demonstrated that the inhibition type was reversible mixed-inhibition with inhibition constants (K_i and K'_i) of 0.431 mM and 0.279 mM, respectively. Furthermore, we put forward a colorimetric method for AMP detection based on nanozyme inhibition. The research on the inhibitory effects of small molecules on nanozymes expands the scope of analysis based on nanozymes and the inhibition mechanism study may offer some insight into investigating the interaction between nanozymes and inhibitors.

Introduction

Due to the high cost and easy inactivation of natural enzymes, exploration of artificial enzymes has always been of great interest. The discovery of peroxidase-like activity of Fe_3O_4 in 2007 by Yan and her colleagues has triggered a huge amount of innovative scientific inquiry.[1] Wei and Wang defined nanozymes as nanomaterials with enzyme-like activities in 2013.[2] Since then, thousands of nanomaterials have been found to have enzyme-mimic activities, such as peroxidase, oxidase, superoxide dismutase, catalase and hydrolase-mimic activities.[3–7] These nanozymes with higher stability and lower cost than natural enzymes are widely used in bioanalysis, antibacterial and cancer treatments, heterogeneous catalysis and pollutant removal, *etc.*[8] However, inherent defects in nanomaterials give rise to low atom utilization and insufficient catalytic activities of nanozymes, in spite of their comparable affinity for substrates to natural enzymes. And the heterogeneity of nano-materials results in the blur of real active sites, which is unfavorable to studying the mechanism of enzyme-like catalysis.[9] The unsatisfactory performances of existing nanozymes raise questions of considerable interest for exploring more efficient materials. Single-atom nanozymes began to arouse researcher's interest in recent years for their maximum atomic utilization efficiency and high intrinsic activity of each active site.[10] Among them, M–N–C (M = metal) was one of the most popular single-atom nanozymes due to its easy preparation and similar active sites to natural enzymes. The similarity of M–N–C structures in single-atom nanozymes with the nitrogen-coordinated metal active sites in natural enzymes endows them with high enzyme-like activities and facilities for mechanism studies.[11]

An important but rarely mentioned part in mechanism studies of nanozymology is nanozyme inhibition. Like the situation of enzyme inhibition, the study of nanozyme inhibition could be used in the fabrication of *turn-off* sensors and the investigation of interactions among nanozymes, substrates and inhibitors. Although nanozymes have been used in a wide range of analysis for health-related small molecules, previous studies simply claimed that the detection mechanism was due to the suppression of enzymatic activities.[12] Few literatures investigated the nanozyme inhibition systematically.[13] And the active sites of previously reported nanoparticles-based nanozymes are usually indeterminate and dissimilar to that of natural enzymes, which makes the mechanism research challenging.[14]

Here, we synthesized Fe–N–C single-atom nanozymes (Fe-SANs) with excellent oxidase-like activity by salt-templated and pyrolytic strategies. The nanosheet morphology of Fe-SANs served the purpose of exposing active sites to obtain high catalytic activity. And FeN_x structures gave their active sites with

[a]State Key Laboratory of Electroanalytical Chemistry, Changchun Institute of Applied Chemistry, Chinese Academy of Sciences, Changchun, Jilin 130022, China
[b]University of Science and Technology of China, Hefei, Anhui 230026, China

† Electronic supplementary information (ESI) available. See DOI: 10.1039/d2sc00212d

high intrinsic activities. The oxidase-like activity of Fe-SANs was found to be inhibited by 4-acetamidophenol (AMP), a common analgesic-antipyretic drug used as a substitution of aspirin. And the inhibitory effects were applied to determine AMP. A moderate amount of AMP has antipyretic and analgesic effects while excessive AMP can cause liver damage.[15] Chromatography and electrochemical sensors were developed for the detection of AMP previously, while colorimetric method for the detection of AMP is rarely reported.[16] Furthermore, we investigated the inhibitory effects of AMP on the oxidase-like activity of Fe-SANs in detail. Michaelis–Menten constant (K_m) and maximum initial velocity (V_m) of Fe-SANs toward TMB in the absence and presence of AMP were obtained by Lineweaver–Burk plots. The type of inhibition induced by AMP was evaluated to be mixed-inhibition of noncompetitive and anticompetitive inhibition. The inhibition constants (K_i and K'_i) were figured out by secondary plotting method.[17] This work may offer some insight into investigating the interaction between nanozymes and inhibitors. And by virtue of the similar active centers to natural enzymes of Fe–N–C single-atom nanozymes, the study on the nanozyme inhibition may provide some basis for the future research on the potential applications of nanozymes in preliminary evaluation and screen of enzyme inhibitors or drugs.[14,18,19]

Results and discussion

Synthesis and characterization of Fe single-atom nanozymes

The Fe single-atom nanozymes (Fe-SANs) were prepared by salt-templated and pyrolytic strategies. Fig. 1a demonstrated the synthetic processes. Briefly, 1,10-phenanthroline monohydrate (*O*-Phen), zinc acetate dihydrate ($Zn(OAc)_2 \cdot 2H_2O$) were dispersed in ethanol. And then mixed with the ethanol solution containing iron (II) phthalocyanine (FePc), followed by the addition of a lot of granular sodium chloride (NaCl). The obtained samples were fully stirred and left to stand at room temperature for 4 h, dried at 75 °C in a vacuum oven and pyrolyzed at 700 °C for 120 min under N_2 atmosphere with heating rate of 5 °C min^{-1}. After that, the samples were washed with H_2O and HCl several times to remove NaCl and possible nanoparticles. In the synthetic process, *O*-Phen was used as N-containing ligand and zinc acetate dihydrate ($Zn(OAc)_2 \cdot 2H_2O$) was introduced to expand the distance of iron (II) phthalocyanine (FePc), separating them from each other during the pyrolysis (Fig. 1a). NaCl particles were employed as hard templates to ensure the formation of nanosheet morphology with large specific surface area. After pyrolysis, the sodium chloride templates were dissolved by water and the possible nanoparticles were removed by pickling to obtain single-atom Fe on nitrogen doped carbon nanosheets. As we can see from Fig. 1b, gauzy nanosheets with wrinkles were obtained thanks to the template role of sodium chloride. SEM image in Fig. S1† also revealed that the nanosheets were micron-sized and thin. Aberration-corrected high angle annular dark-field scanning transmission electron microscope (HAADF-STEM) image (Fig. 1c) of Fe-SANs indicated that Fe atoms dispersed on the nanosheets separately, and no nanoparticles were observed. Energy dispersive X-ray spectroscopy (EDS) elemental analysis (Fig. 1d) demonstrated the homogeneous dispersion of C, N and Fe on the nanosheets. The XRD patterns Fe-SANs preliminarily manifested the atomically dispersion of Fe (Fig. S2†). The only two diffraction peaks in XRD patterns were attributed to graphite and no peaks of Fe nanoparticles were observed.[20] The iron content in the Fe-SANs is 0.028%, measured by inductively coupled plasma massspectrometry (ICP-MS).

Raman spectra in Fig. 2a demonstrated two major peaks at 1352.3 cm^{-1} and 1587.1 cm^{-1} belonging to D band and G band of graphite. I_D/I_G was 1.15, where I_D and I_G represented the intensities of the D band and G band respectively.[21] X-ray photoelectron spectroscopy (XPS) confirmed the presence of C, N and O (Fig. S3†), consistent with the EDS mappings. No Fe species was observed because of the low sensitivity of XPS and the small amount of Fe in the single-atom nanozymes. The N 1s XPS spectra (Fig. 2b) could be fitted to four peaks at 398.27 eV, 399.78 eV, 400.84 eV and 402.42 eV, which were attributed to pyridinic-N, pyrrolic-N, graphitic-N and oxidic-N respectively.[22] The N species in Fe-SANs played important roles in iron coordination. Furthermore, X-ray absorption fine structure spectra (XAFS) were employed to investigate the local structure of Fe in atomic level. Fig. 2c showed the Fe K-edge X-ray absorption near edge structure spectra (XANES) of Fe-SANs and other references. The near-edge adsorption energy of Fe-SANs was sandwiched between Fe foil and Fe_2O_3, indicating the valence state of iron in Fe-SANs was 0 to +3.[23] Extended X-ray absorption fine structure spectra (EXAFS) of Fe-SANs and other references in *r*-space were shown in Fig. 2d. The peaks at $R = 2.21$ Å and $R = 2.55$ Å were attributed to Fe–Fe scattering path in Fe foil and Fe_2O_3 respectively and no corresponding peaks were shown in Fe-

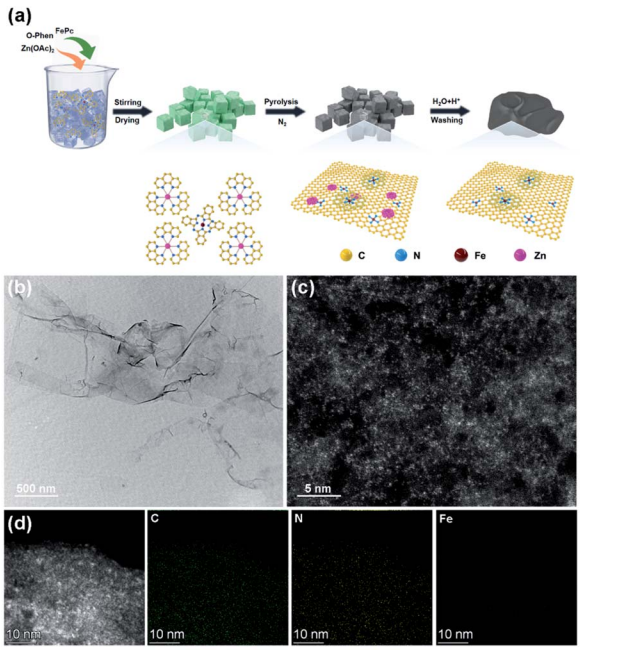

Fig. 1 (a) Schematic diagram of salt-templated and pyrolytic strategies to synthesize Fe-SANs. (b) TEM, (c) HAADF-STEM image and (d) corresponding EDS mappings of Fe single-atom nanozymes (Fe-SANs).

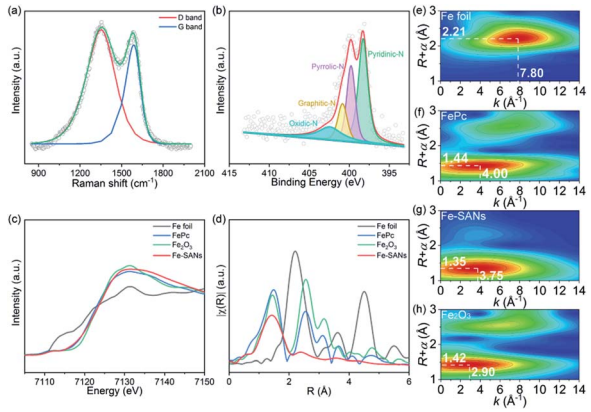

Fig. 2 (a) Raman spectra, (b) XPS N1s spectra of Fe-SANs. (c) Fe K-edge XANES spectra and (d) Fourier transformations of Fe K-edge EXAFS in *r*-space. (e)–(h) Wavelet transforms of Fe K-edge EXAFS of Fe foil, FePc, Fe-SANs and Fe_2O_3.

SANs, indicating the absence of metallic Fe or FeO_x nanoparticles. The dominating peak at $R = 1.41$ Å in Fe-SANs was approximate to the peaks at 1.47 Å in FePc and 1.44 Å in Fe_2O_3. Wavelet transform was employed to distinguish atoms with similar distances to absorbing atom according to their elemental nature. Wavelet analysis could provide information in both *k*-space and *r*-space.[24] Fig. 2e–h demonstrated the wavelet transforms of the EXAFS for Fe foil, FePc, Fe-SANs and Fe_2O_3 respectively. The contour plots of Fe- SANs showed maximum intensity at $R = 1.35$ Å and $k = 3.75$ Å^{-1}, which was aligned well with FePc at $R = 1.44$ Å and $k = 4.00$ Å^{-1} but distinct with Fe_2O_3 at $R = 1.42$ Å and $k = 2.90$ Å^{-1}. The contour plots obtained from wavelet transforms suggested the Fe–N coordination in Fe-SANs.[25] The FeN_x structures in Fe-SANs were expected to exhibit superior oxidase-like activity.

The oxidase-like activity of Fe-SANs and inhibition of AMP

To assess the oxidase-like activity of Fe-SANs, TMB was used as a substrate for its obvious color change after oxidation and characteristic absorbance at 652 nm of oxidative product oxTMB. As we can see from Fig. 3a, the air-saturated solution containing TMB turned blue and an absorption peak at 652 nm appeared in the presence of Fe-SANs. The absorbance increased in O_2-saturated buffer solution and decreased in N_2-saturated buffer solution, which indicated the key role of O_2 in the oxidation of TMB (Fig. S4†). The coexist of only O_2 and TMB showed no change in the absorbance at 652 nm, demonstrating the oxidase-like activity of Fe-SANs in the catalytic oxidation of TMB. The nitrogen doped carbon nanosheets prepared without addition of FePc showed extremely low activity (Fig. S5†), indicating that the oxidase-like activity of Fe-SANs was derived from the Fe sites in the nanosheets. The oxidase-like activity of Fe-SANs changed with pH and had a highest activity at pH 3.0 (Fig. S6a†). They exhibited high activities in a wide temperature range, performing better than natural enzymes (Fig. S6b†). The steady-state kinetics of Fe-SANs were analyzed by measuring the initial velocities at varied TMB concentrations. The plots fitted well with typical Michaelis–Menten curves (Fig. 3e, black line). We derived the Michaelis–Menten constant (K_m) to be 0.114 mM and maximum initial velocity (V_m) with 10 μg mL^{-1} Fe-SANs to be 6.5×10^{-8} M s^{-1} from the Lineweaver–Burk plots. The catalytic rate constant (k_{cat}) and the catalytic efficiency k_{cat}/K_m were 1.3 s^{-1} and 11.4 mM^{-1} s^{-1}, respectively. We compared the kinetic parameters with other iron-based nanozymes in Table S1.† The smaller K_m of Fe-SANs than other reported nanozymes means higher affinity for substrates. Since the maximum initial velocity is related to the concentration of nanozymes, it is improper to compare the maximum initial velocity without mentioning the nanozymes concentration. We compared k_{cat} instead of directly comparing V_m. According to Table S1,† the k_{cat} of Fe-SANs was substantially higher than most of the reported nanozymes, including single-atom nanozymes, which meant higher catalytic efficiency of Fe-SANs. To study the mechanism for showing oxidase-like activity of Fe-SANs, we take electron paramagnetic resonance (EPR) experiments. As shown in Fig. S7,† no signals of $\cdot O_2^-$ and ·OH were detectable, while the signal intensity of $^1O_2$ was strong. We believe that the oxidase-like activity of Fe-SANs is derived from the $^1O_2$ produced from O_2.

In addition, we found that the absorbance at 652 nm of TMB catalyzed by Fe-SANs decreased in the presence of 4-acetamidophenol (AMP). The time-dependent absorbance at 652 nm of TMB changed more slowly with the increase of AMP concentration, meaning the inhibitory effects of AMP on the oxidase-like activity of Fe-SANs (Fig. 3b). The initial velocities for TMB oxidation showed linear relation with the concentrations of Fe-SANs (Fig. 3c). In the presence of AMP, the straight lines passed through the origin with decreasing slope, which was a characteristic of reversible inhibition. To further study the inhibitory effects of AMP on Fe-SANs, we measured the initial velocities at varied TMB concentrations in the presence of AMP. As described in Fig. 3e, the catalytic kinetics followed with Michaelis–Menten curves as well. The Lineweaver–Burk plots at different AMP concentrations intersected at a point in the third quadrant, suggesting that the AMP mediated inhibition of the oxidase-like activity was a result of mixed-inhibition.[17,26] The Michaelis–Menten constant and maximum initial velocity in the presence of inhibitors were represented by K_m^I and V_m^I, where *I* referred to AMP inhibitors. K_m^I and V_m^I were obtained from the Lineweaver–Burk plots and listed in Table S2.† Both the Michaelis–Menten constant and maximum initial velocity decreased with the increase of AMP concentration. The inhibitor constants (K_i and K'_i), that is to say the dissociation constants of EI (nanozymes and inhibitors) or EIS (nanozymes, inhibitors and substrates), were obtained from the relationship curves between K_m^I/V_m^I or $1/V_m^I$ and [*I*] (inhibitor concentration) (Fig. S8,† eqn (1)). Plot K_m^I/V_m^I against [*I*] to obtain the relationship curve with a slope as $\frac{K_m}{V_m K_i}$, and K_i was figured out to be 0.431 mM. In the same way, the slope of relationship curve between $1/V_m^I$ and [*I*] was $\frac{1}{V_m K'_i}$, and K'_i was derived to be

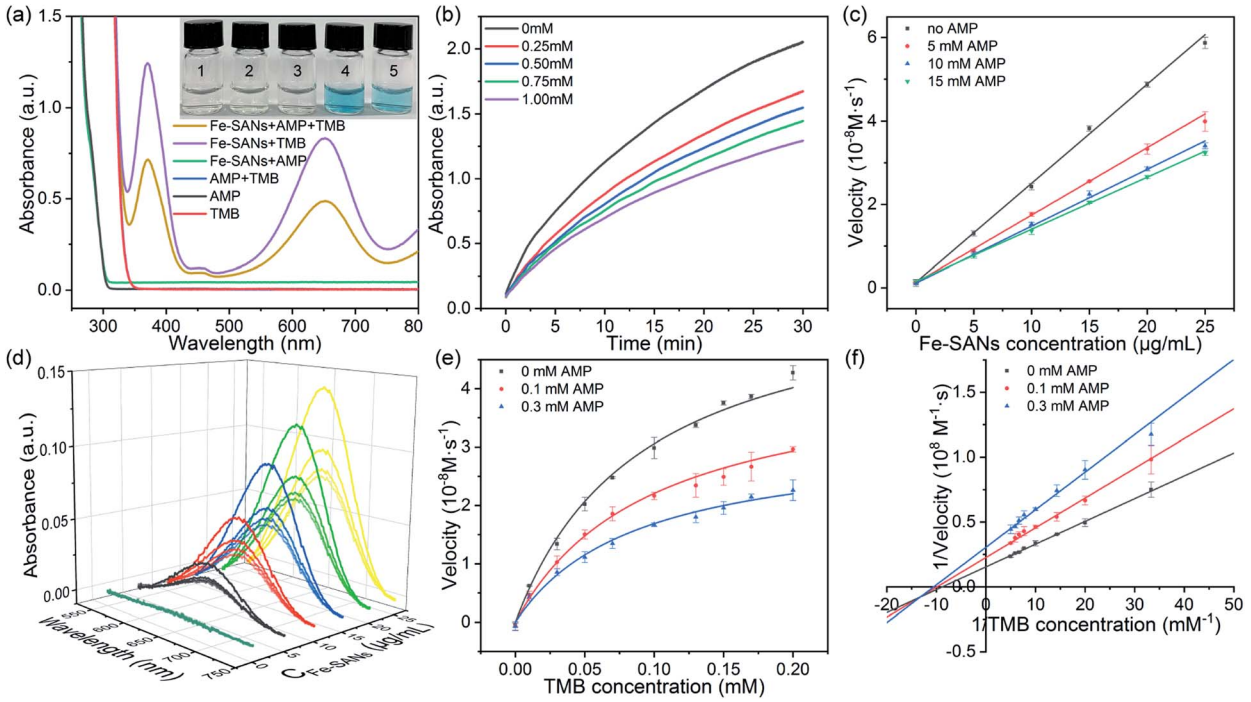

Fig. 3 The oxidase-like activity of Fe-SANs and inhibition of AMP. (a) The UV-vis absorption spectra of TMB and AMP with or without Fe-SANs in air-saturated buffer (inset: digital photos of (1) TMB, (2) TMB + AMP, (3) Fe-SANs + AMP, (4) Fe-SANs + TMB and (5) Fe-SANs + AMP + TMB solutions after mixing for 5 min). (b) Time-dependent absorbance at 652 nm of TMB with 10 μg mL^{-1} Fe-SANs and different concentration of AMP. (c) The initial velocities of TMB oxidation and (d) corresponding UV-vis absorption spectra at different AMP concentrations vary with Fe-SANs concentration. (e) Michaelis–Menten curves and (f) Lineweaver–Burk plots of TMB oxidation at different AMP concentrations.

0.279 mM. $K_i > K'_i$ indicated that AMP had a higher affinity to the complexes of Fe-SANs and substrates than free Fe-SANs.[17] The inhibition type was noncompetitive inhibition and anti-competitive inhibition according to the position of the intersection and the values of K_i and K'_i.

The detection of AMP based on nanozyme inhibition

AMP is used as an analgesic and antipyretic drug in treatment, but excessive ingestion of AMP results in liver damage and even brain damage.[15] However, the previously reported chromatography, high performance liquid chromatography and electrochemical sensors always require certain equipment or complex processes. Developing a handy method for the determination of AMP is of great significance. We proposed a colorimetric method for AMP detection based on the inhibitory effects of AMP on Fe-SANs. The detection mechanism was illustrated in Fig. 4a. Fe-SANs could combine with TMB and then AMP, *vice versa*. TMB combined with free Fe-SANs and the complexes of Fe-SANs and AMP (Fe-SANs/AMP) to form Fe-SANs/TMB and AMP/Fe-SANs/TMB respectively. However, AMP/Fe-SANs/TMB couldn't generate products (oxTMB) directly, which led to the decrease of absorbance at 652 nm. The absorbance of TMB decreased while the concentration of AMP increased and exhibited a linear relation at 0.03–0.4 mM. The limit of detection (LOD) was 3.23 μM at a signal-to-noise ratio of 3. We applied the method to the determination of AMP in commercial paracetamol tablets and obtained proper recovery with small relative standard deviation (Table S3†). And by virtue of the superior activities of Fe-SANs, this method is fast enough for actual detection. These results suggested that Fe-SANs showed the possibility to determine AMP in actual sample. However, sensor arrays may be required to achieve selectivity in the coexistence of a variety of analytes with similar properties.

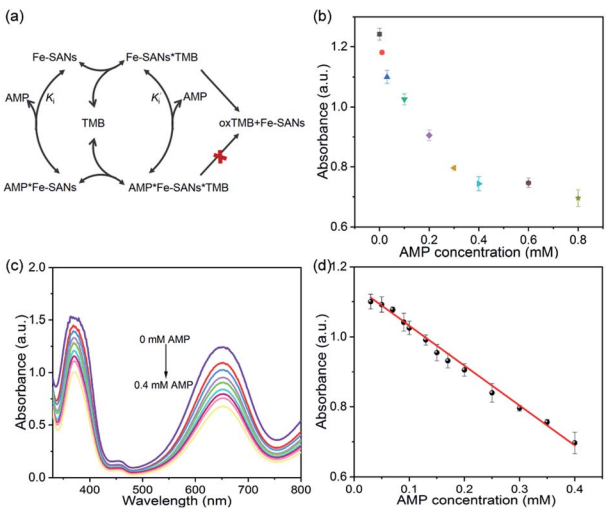

Fig. 4 (a) The catalytic mechanism of AMP determination. (b) Absorbance at 652 nm and (c) UV-vis absorption spectra of TMB at different AMP concentrations. (d) Linear relationship between absorbance at 652 nm and AMP concentrations.

Conclusions

In summary, we prepared single-atom Fe nanozymes by salt-templated and pyrolytic strategies. Benefit from the large specific surface area of carbon nanosheets, maximum atomic utilization efficiency of single-atom nanomaterials and high intrinsic activities of FeN_x sites, the prepared Fe-SANs exhibited ultrahigh oxidase-like activity. The oxidase-like activity of Fe-SANs would be suppressed to a certain extent in the presence of AMP. Based on the inhibitions, a colorimetric method for AMP detection was proposed. Furthermore, we investigated the inhibition type and mechanism detailedly by measuring the kinetics of TMB oxidation in the absence and presence of AMP. The inhibition type was proved to be a mix of noncompetitive inhibition and anticompetitive inhibition. Our research on the inhibitory effects of small molecules on nanozymes are expected to provide the basis for studying the interaction between nanozymes and inhibitors and *in vitro* inhibitors pre-screening.

Experimental section

Preparation of Fe-SANs

The Fe-SANs were prepared by salt-templated and pyrolytic strategies. Specifically, 30 mg $Zn(OAc)_2 \cdot 2H_2O$ and 100 mg 1,10-phenanthroline monohydrate were dissolved in 3.5 mL ethanol. 100 μL HCl was diluted with 1 mL H_2O and mixed with the solution mentioned above. Subsequently, 1.5 mL 2 mg mL^{-1} FePc dispersed in ethanol were introduced. The obtained precursor solution was mixed with 30 g NaCl evenly after vigorous stirring. The mixtures were left to stand at room temperature for 4 h, dried at 75 °C in a vacuum oven and pyrolyzed at 700 °C for 120 min under N_2 atmosphere with heating rate of 5 °C min^{-1}. And then, the samples were washed with H_2O and 1 M HCl for five times to remove NaCl and possible nanoparticles.

Analysis of oxidase-like activity of Fe-SANs

The oxidase-like activity of Fe-SANs was measured by collecting the absorbance of oxidized TMB at 652 nm. The steady-state kinetic assays were carried out in 1.0 mL air-saturated sodium acetate buffer (0.1 M, pH 3.0) with TMB concentrations from 0 to 0.2 mM in the presence of 10 μg mL^{-1} Fe-SANs. The obtained curves of V *vs.* C_{TMB} followed Michaelis–Menten kinetics, and the kinetics parameters could be calculated from Lineweaver–Burk plots according to $1/V_m = K_m/V_m \times 1/[S]+1/V_m$.

Inhibitory effects of 4-acetamidophenol on the oxidase-like activity of Fe-SANs

We investigated the inhibitory effects of 4-acetamidophenol on the oxidase-like activity of Fe-SANs by measuring the residual activity in the presence of 4-acetamidophenol. The initial velocities of TMB oxidation varies with Fe-SANs concentration were measured by changing the concentrations of Fe-SANs from 0 to 25 μg mL^{-1} while keeping TMB concentration as 0.5 mM. The same procedures were carried out at three AMP concentrations (5 mM, 10 mM and 15 mM) to investigate the influence of AMP. The steady-state kinetics of Fe-SANs toward TMB in the presence of AMP were investigated by varying TMB concentrations while keeping AMP and Fe-SANs at fixed concentrations. The Michaelis constant (K_m^I) and maximum reaction velocity (V_m^I) in the presence of different concentrations of inhibitors were obtained from Lineweaver–Burk plots. Subsequently, we could decide the inhibition type to be mixed-inhibition according to Lineweaver–Burk graphical methods and the comparison of Michaelis constants and maximum reaction velocities with that in the absence of inhibitors.[17] The Michaelis–Menten equation of mixed-inhibition system could be expressed by eqn (1):

$$\frac{1}{V} = \frac{K_m}{V_m} \times \frac{1}{S}(1 + [I]/K_i) + \frac{1}{V_m}\left(1 + [I]/K'_i\right) \quad (1)$$

The relationship among K_m^I, $V_m{}^I$ and $[I]$ could be described as $\frac{K_m^I}{V_m^I} = \frac{K_m}{V_m}(1 + [I]/K_i)$, and $\frac{1}{V_m^I} = \frac{1}{V_m}(1 + [I]/K'_i)$, $[I]$ referred to the concentration of AMP. The slope of curves $K_m{}^I/V_m^I \sim [I]$ and $1/V_m^I \sim [I]$ were $\frac{K_m}{V_m K_i}$ and $\frac{1}{V_m K'_i}$ respectively. Therefore, we could derive K_i and K'_i by the secondary plotting method.

Colorimetric detection of 4-acetamidophenol

AMP coexisted with TMB made the oxidization of TMB slacken, accompanied by significantly reduced absorbance. The absorbance of oxidized TMB in the presence of different concentrations AMP was measured to determine the concentration of AMP. Specifically, 20 μL 0.5 mg mL^{-1} Fe-SANs, 20 μL 40 mM TMB were added to 960 μL sodium acetate buffer (0.1 M, pH 3.0) containing different concentrations of AMP. The absorbance at 652 nm was measured after 10 min reaction at room temperature.

Data availability

The data supporting the findings of this study are available within the article and in the ESI.†

Author contributions

W. Wu led the conceptualization, investigation of this work and the writing of original draft. L. Huang supported the conceptualization and supervision. X. Zhu helped the data analysis. J. Chen and D. Chao helped the investigation. M. Li and S. Wu supported the writing of original draft. S. Dong helped the supervision and led the review & editing.

Conflicts of interest

There are no conflicts to declare.

Acknowledgements

We are grateful for the support from the Ministry of Science and Technology of China (No. 2016YFA0203203, 2019YFA0709202), the National Natural Science Foundation of China (No. 22074137).

Notes and references

1 L. Gao, J. Zhuang, L. Nie, J. Zhang, Y. Zhang, N. Gu, T. Wang, J. Feng, D. Yang, S. Perrett and X. Yan, *Nat. Nanotechnol.*, 2007, **2**, 577–583.

2 H. Wei and E. Wang, *Chem. Soc. Rev.*, 2013, **42**, 6060–6093.

3 (*a*) Z. Dai, S. Liu, J. Bao and H. Jui, *Chem.–Eur. J.*, 2009, **15**, 4321–4326; (*b*) D. Feng, Z.-Y. Gu, J.-R. Li, H.-L. Jiang, Z. Wei and H.-C. Zhou, *Angew. Chem., Int. Ed.*, 2012, **51**, 10307–10310; (*c*) M. S. Kim, S. Cho, S. H. Joo, J. Lee, S. K. Kwak, M. I. Kim and J. Lee, *Acs Nano*, 2019, **13**, 4312–4321; (*d*) M. K. Masud, S. Yadav, M. N. Isam, N. T. Nguyen, C. Salomon, R. Kline, H. R. Alamri, Z. A. Alothman, Y. Yamauchi, M. S. A. Hossain and M. J. A. Shiddiky, *Anal. Chem.*, 2017, **89**, 11005–11013; (*e*) R. Bhattacharjee, S. Tanaka, S. Moriam, M. K. Masud, J. Lin, S. M. Alshehri, T. Ahamad, R. R. Salunkhe, N. T. Nguyen, Y. Yamauchi, M. S. A. Hossain and M. J. A. Shiddiky, *J. Mater. Chem. B*, 2018, **6**, 4783–4791; (*f*) M. K. Masud, J. Kim, M. M. Billah, K. Wood, M. J. A. Shiddiky, N. T. Nguyen, R. K. Parsapur, Y. V. Kaneti, A. A. Alshehri, Y. G. Alghamidi, K. A. Alzahrani, M. Adharvanachari, P. Selvam, M. S. A. Hossain and Y. Yamauchi, *J. Mater. Chem. B*, 2019, **7**, 5412–5422.

4 (*a*) S. Bhattacharyya, S. R. Ali, M. Venkateswarulu, P. Howlader, E. Zangrando, M. De and P. S. Mukherjee, *J. Am. Chem. Soc.*, 2020, **142**, 18981–18989; (*b*) J. Wu, Z. Wang, X. Jin, S. Zhang, T. Li, Y. Zhang, H. Xing, Y. Yu, H. Zhang, X. Gao and H. Wei, *Adv. Mater.*, 2021, **33**, 2005024.

5 Y. Li, X. He, J.-J. Yin, Y. Ma, P. Zhang, J. Li, Y. Ding, J. Zhang, Y. Zhao, Z. Chai and Z. Zhang, *Angew. Chem., Int. Ed.*, 2015, **54**, 1832–1835.

6 (*a*) X. Liu, Z. Zhang, Y. Zhang, Y. Guan, Z. Liu, J. Ren and X. Qu, *Adv. Funct. Mater.*, 2016, **26**, 7921–7928; (*b*) J. Fan, J.-J. Yin, B. Ning, X. Wu, Y. Hu, M. Ferrari, G. J. Anderson, J. Wei, Y. Zhao and G. Nie, *Biomaterials*, 2011, **32**, 1611–1618.

7 (*a*) J. Chen, L. Huang, Q. Wang, W. Wu, H. Zhang, Y. Fang and S. Dong, *Nanoscale*, 2019, **11**, 5960–5966; (*b*) T. Fu, C. Xu, R. Guo, C. Lin, Y. Huang, Y. Tang, H. Wang, Q. Zhou and Y. Lin, *ACS Appl. Nano Mater.*, 2021, **4**, 3345–3350.

8 (*a*) J. Wu, X. Wang, Q. Wang, Z. Lou, S. Li, Y. Zhu, L. Qin and H. Wei, *Chem. Soc. Rev.*, 2019, **48**, 1004–1076; (*b*) Q. Wang, H. Wei, Z. Zhang, E. Wang and S. Dong, *TrAC, Trends Anal. Chem.*, 2018, **105**, 218–224; (*c*) S.-R. Li, Y.-C. Huang, J.-R. Liu, E.-K. Wang and H. Wei, *Prog. Biochem. Biophys.*, 2018, **45**, 129–147; (*d*) M. K. Masud, J. Na, M. Younus, M. S. A. Hossain, Y. Bando, M. J. A. Shiddiky and Y. Yamauchi, *Chem. Soc. Rev.*, 2019, **48**, 5717–5751.

9 (*a*) L. Jiao, H. Yan, Y. Wu, W. Gu, C. Zhu, D. Du and Y. Lin, *Angew. Chem., Int. Ed.*, 2020, **59**, 2565–2576; (*b*) H. Zhang, X. F. Lu, Z.-P. Wu and X. W. D. Lou, *ACS Cent. Sci.*, 2020, **6**, 1288–1301.

10 (*a*) L. Huang, J. Chen, L. Gan, J. Wang and S. Dong, *Sci. Adv.*, 2019, **5**, eaav5490; (*b*) B. Xu, H. Wang, W. Wang, L. Gao, S. Li, X. Pan, H. Wang, H. Yang, X. Meng, Q. Wu, L. Zheng, S. Chen, X. Shi, K. Fan, X. Yan and H. Liu, *Angew. Chem., Int. Ed.*, 2019, **58**, 4911–4916; (*c*) X. Xie, D. P. Wang, C. Guo, Y. Liu, Q. Rao, F. Lou, Q. Li, Y. Dong, Q. Li, H. B. Yang and F. X. Hu, *Anal. Chem.*, 2021, **93**, 4916–4923; (*d*) Y. Wang, K. Qi, S. Yu, G. Jia, Z. Cheng, L. Zheng, Q. Wu, Q. Bao, Q. Wang, J. Zhao, X. Cui and W. Zheng, *Nano-Micro Lett.*, 2019, **11**, 102.

11 (*a*) M. S. Kim, J. Lee, H. S. Kim, A. Cho, K. H. Shim, T. N. Le, S. S. A. An, J. W. Han, M. I. Kim and J. Lee, *Adv. Funct. Mater.*, 2020, **30**, 1905410; (*b*) L. Jiao, W. Xu, H. Yan, Y. Wu, C. Liu, D. Du, Y. Lin and C. Zhu, *Anal. Chem.*, 2019, **91**, 11994–11999.

12 (*a*) Q. Chen, S. Li, Y. Liu, X. Zhang, Y. Tang, H. Chai and Y. Huang, *Sens. Actuators, B*, 2020, **305**, 127511; (*b*) Y. Wu, L. Jiao, X. Luo, W. Xu, X. Wei, H. Wang, H. Yan, W. Gu, B. Z. Xu, D. Du, Y. Lin and C. Zhu, *Small*, 2019, **15**, 1903108; (*c*) W. Song, B. Zhao, C. Wang, Y. Ozaki and X. Lu, *J. Mater. Chem. B*, 2019, **7**, 850–875.

13 (*a*) H. Jia, D. Yang, X. Han, J. Cai, H. Liu and W. He, *Nanoscale*, 2016, **8**, 5938–5945; (*b*) D.-F. Chai, Z. Ma, Y. Qiu, Y.-G. Lv, H. Liu, C.-Y. Song and G.-G. Gao, *Dalton Trans.*, 2016, **45**, 3048–3054; (*c*) L. Su, X. Yu, Y. Cai, P. Kang, W. Qin, W. Dong, G. Mao and S. Feng, *Anal. Chim. Acta*, 2017, **987**, 98–104; (*d*) J. Liu, X. Hu, S. Hou, T. Wen, W. Liu, X. Zhu and X. Wu, *Chem. Commun.*, 2011, **47**, 10981–10983; (*e*) M. Singh, P. Weerathunge, P. D. Liyanage, E. Mayes, R. Ramanathan and V. Bansal, *Langmuir*, 2017, **33**, 10006–10015.

14 Y. Xu, J. Xue, Q. Zhou, Y. Zheng, X. Chen, S. Liu, Y. Shen and Y. Zhang, *Angew. Chem., Int. Ed.*, 2020, **59**, 14498–14503.

15 M. T. Olaleye and B. T. J. Rocha, *Exp. Toxicol. Pathol.*, 2008, **59**, 319–327.

16 W. Zhang, L. Zong, S. Liu, S. Pei, Y. Zhang, X. Ding, B. Jiang and Y. Zhang, *Biosens. Bioelectron.*, 2019, **131**, 200–206.

17 (*a*) H. Lineweaver and D. Burk, *J. Am. Chem. Soc.*, 1934, **56**, 658–666; (*b*) F. Arduini, A. Amine, D. Moscone and G. Palleschi, *Anal. Lett.*, 2009, **42**, 1258–1293.

18 (*a*) M. Chaudhary, V. Singh, A. R. Anvikar and S. Sahi, *Curr. Comput.-Aided Drug Des.*, 2016, **12**, 282–293; (*b*) N. E. Labrou, *Methods Mol. Biol.*, Springer, 2020,p. 2089.DOI: DOI: 10.1007/978-1-0716-0163-1.

19 A. Amine, F. Arduini, D. Moscone and G. Palleschi, *Biosens. Bioelectron.*, 2016, **76**, 180–194.

20 W. Ma, J. Mao, X. Yang, C. Pan, W. Chen, M. Wang, P. Yu, L. Mao and Y. Li, *Chem. Commun.*, 2019, **55**, 159–162.

21 P. Pachfule, D. Shinde, M. Majumder and Q. Xu, *Nat. Chem.*, 2016, **8**, 718–724.

22 (*a*) Y. Hu, X. J. Gao, Y. Zhu, F. Muhammad, S. Tan, W. Cao, S. Lin, Z. Jin, X. Gao and H. Wei, *Chem. Mater.*, 2018, **30**,

6431–6439; (*b*) F. Pan, J. Jin, X. Fu, Q. Liu and J. Zhang, *ACS Appl. Mater. Interfaces*, 2013, **5**, 11108–11114.

23 (*a*) C. Zhao, C. Xiong, X. Liu, M. Qiao, Z. Li, T. Yuan, J. Wang, Y. Qu, X. Wang, F. Zhou, Q. Xu, S. Wang, M. Chen, W. Wang, Y. Li, T. Yao, Y. Wu and Y. Li, *Chem. Commun.*, 2019, **55**, 2285–2288; (*b*) B. Ravel and M. Newville, *J. Synchrotron Radiat.*, 2005, **12**, 537–541.

24 (*a*) H. Funke, A. C. Scheinost and M. Chukalina, *Phys. Rev. B: Condens. Matter Mater. Phys.*, 2005, **71**, 094110; (*b*) H. Funke, M. Chukalina and A. C. Scheinost, *J. Synchrotron Radiat.*, 2007, **14**, 426–432.

25 M. Huo, L. Wang, Y. Wang, Y. Chen and J. Shi, *Acs Nano*, 2019, **13**, 2643–2653.

26 T. Xiao, X. Y. Xie, C. Bin Xue, W. C. Luo, L. Jiang and S. Cao, *Pestic. Biochem. Physiol.*, 2008, **91**, 39–44.